



## Article

# The Variations of Outgoing Longwave Radiation in East Asia and Its Influencing Factors

Chaoli Tang <sup>1,2</sup>, Dong Liu <sup>1,\*</sup>, Xiaomin Tian <sup>1</sup>, Fengmei Zhao <sup>1</sup> and Congming Dai <sup>3,4,\*</sup>

<sup>1</sup> School of Electrical & Information Engineering, Anhui University of Science and Technology, Huainan 232001, China; chltang@mail.ustc.edu.cn (C.T.)

<sup>2</sup> State Key Laboratory of Space Weather, Chinese Academy of Sciences, Beijing 100190, China

<sup>3</sup> Key Laboratory of Atmospheric Optics, Anhui Institute of Optics and Fine Mechanics, Chinese Academy of Sciences, Hefei 230031, China

<sup>4</sup> Advanced Laser Technology Laboratory of Anhui Province, Hefei 230037, China

\* Correspondence: 2020200697@aust.edu.cn (D.L.); cmdai@aiofm.ac.cn (C.D.)

**Abstract:** Outgoing longwave radiation (OLR) data are one of the key factors in studying the radiation balance of the earth–atmosphere system in East Asia. It is of great significance to explore the influence factors on OLR. This paper processes the data of nearly 19 years, from September 2002 to February 2022, and conducts in-depth research using the exponential smoothing method, empirical orthogonal decomposition (EOF), correlation analysis, and other methods. We found that the spatial distribution of OLR is zonal symmetry and gradually decreases with the increase of latitude. Using EOF analysis, it is found that the total variance contribution of the first four decomposed spatial features exceeds 70%, and the overall change trend of the four-time coefficients in the past 19 years all show a downward trend. OLR is positively correlated with total column water vapor (TCWV), air temperature (AT), and cloud top temperature (CTT), but negatively correlated with cloud top pressure (CTP). OLR has a similar spatial correlation distribution with TCWV and AT, while the spatial correlation between OLR and CTP is opposite to the first two parameters. In most parts of East Asia, the spatial correlation with CTT exceeds 0.8. The change in OLR value is affected by various meteorological parameters. In East Asia, the positive correlation between 30° N and 60° N is significantly affected by TCWV, AT, and CTT; and the negative correlation is more significantly affected by CTP. At 0–25° N, the positive correlation is significantly affected by CTP and CTT, while the negative correlation is significantly affected by TCWV and AT.

**Keywords:** atmospheric infrared sounder; East Asia; outgoing longwave radiation; spatiotemporal distribution; correlation analysis



**Citation:** Tang, C.; Liu, D.; Tian, X.; Zhao, F.; Dai, C. The Variations of Outgoing Longwave Radiation in East Asia and Its Influencing Factors. *Atmosphere* **2023**, *14*, 576. <https://doi.org/10.3390/atmos14030576>

Academic Editors: Fei Yang, Lei Wang and Qingzhi Zhao

Received: 30 January 2023

Revised: 3 March 2023

Accepted: 15 March 2023

Published: 17 March 2023



**Copyright:** © 2023 by the authors. Licensee MDPI, Basel, Switzerland. This article is an open access article distributed under the terms and conditions of the Creative Commons Attribution (CC BY) license (<https://creativecommons.org/licenses/by/4.0/>).

## 1. Introduction

The law of conservation of energy is bound to exist in the process of development of things. In addition, in atmospheric scientific research, it is found that the energy of the sun shining on the earth and the energy reflected in space by the earth are in balance. This energy balance promotes the formation of the earth's climate and development [1]. In this paper, we used outgoing longwave radiation (OLR) data detected by an atmospheric infrared sounder (AIRS) to study their related influencing factors [2]. OLR refers to the energy of electromagnetic waves of all wavelengths radiated by the earth to outer space, which can reflect the energy radiation of the earth–atmosphere system and is affected by the surface temperature, atmospheric temperature, cloud amount, etc. It can be regarded as an indicator of energy status [3]. Especially in low latitudes, it is widely used in the research of abnormal climate, weather forecast analysis, air–sea interaction, etc. [4].

The improvement and utilization of satellite data acquisition methods greatly complement the insufficiency of conventional detection methods in tropical regions [5], providing

conditions for studying global climate change and anomalies. Understanding and re-searching OLR data can provide a large amount of information on tropical oceans and atmospheres [6,7]. The study of its correlation characteristics, spatiotemporal variation, and inter-annual changes can better understand the changes in the earth-atmosphere system in the tropical ocean region [8]. At the same time, the research on influencing factors of OLR is also beneficial to understand the influence of abnormal weather on the changes in the whole sea area [9].

The distribution and changes of OLR are affected by many factors [10], such as latitude, season, cloud, precipitation, ground-effective radiation, underlying surface, and atmospheric temperature, of which latitude and seasonal influence determine the basic trend that OLR, cloud, precipitation, underlying surface, and atmospheric temperature, etc. will make deviate [11]. Therefore, many scholars have researched the variation characteristics, influencing factors, and the relationship between abnormal weather and OLR in the plateau area. However, what about the trends in different seasons and regions? What are the factors that affect its distribution and change? All are issues worthy of further study and improvement. This paper explores the spatiotemporal characteristics of OLR and makes a simple prediction of its future changes. Due to the rise of air temperature (AT) caused by human activities, total column water vapor (TCWV) [12] rises, the cloud top pressure (CTP) [13], and cloud top temperature (CTT) [14] change; and, ultimately, affect the change of OLR. So, studies on the correlation between OLR and TCWV, AT, CTP, and CTT are of high research significance and novelty.

We compared previous studies, such as Koji, AK, et al. [15], who studied the spatiotemporal distribution of water vapor; Amoruso, A, et al. [16] used the EOF method to study the characteristics of the volcanic system; and Zhang, TQ, et al. [17] used correlation to analyze the permafrost of the Qinghai-Tibet Plateau for many years. This paper aims to use the OLR data detected by AIRS, first studied its spatiotemporal distribution, and understand the laws of its spatiotemporal changes. Then the exponential smoothing method is used to predict its time, and the EOF method is used to analyze its spatial characteristics. Finally, the potential influencing factors are studied.

## 2. Datasets and Methods

### 2.1. Datasets

This paper uses data detected by the atmospheric infrared sounder (AIRS) on the Aqua satellite launched in 2002 for research [18,19]. The level-3 data contains TCWV, temperature, O<sub>3</sub>, OLR, and other parameters of the entire troposphere [20]. Its spatial resolution is 1 deg. (longitude) × 1 deg. (latitude), and it transits the mid-latitude region twice a day [21]. The main research area of this paper is East Asia, and the research area is 0~60° N and 70~160° E [22–24]. It mainly includes China, North Korea, South Korea, Japan, Mongolia, and part of the western Pacific Ocean, as well as the Qinghai-Tibet Plateau, the third pole in the world. Meanwhile, it includes land, ocean, plateau, and other environmental areas. This area can provide a sufficient basic value for understanding the distribution and changing trend of OLR. Because satellite data can cover a large area of the world, can be scanned continuously, and are less disturbed by other human factors, many researchers used satellite remote sensing for research [25]. In this paper, we used the data of OLR, TCWV, AT, CTP, and CTT detected by AIRS remote sensing for research. At the same time, all the data used in this paper were verified by experiments, and it is found that no data are missing, which can be used for research. In this paper, the OLR is carried out month by month, year-by-year, and seasonal change to study [26]. Then, the inter-annual variation of each latitude segment in East Asia is studied, and some parameters that can cause OLR changes, such as TCWV, AT, CTP, and CTT, are also studied.

## 2.2. Methods

### 2.2.1. Exponential Smoothing Methods

The exponential smoothing method uses the actual value of the previous period and the predicted value of the previous period, supplemented by a smoothing coefficient, to calculate the predicted value [27]. In practical applications, the prediction model is highly adaptable, it can automatically identify data changes, and make adjustments. At the same time, there are many kinds of exponential smoothing methods. For example, the first-order exponential smoothing method is often used for time series that do not have obvious function rules but have some connection. The first-order exponential smoothing method principle is as follows:

$$\hat{y}_t = \alpha \cdot y_t + (1 - \alpha) \cdot \hat{y}_{t-1} \tag{1}$$

In the formula, alpha represents the smoothing factor, which defines how fast we can “forget” the current real observations. Alpha: the smaller the influence of the current real observation value, the greater the influence of the predicted value of the previous model, and the smoother the final time series will be.

Linear time series usually use the double-exponential smoothing method. The double-exponential smoothing method principle formula is as follows:

$$l_x = \alpha y_x + (1 - \alpha)(l_{x-1} + b_{x-1}) \tag{2}$$

$$b_x = \beta(l_x - l_{x-1}) + (1 - \beta)b_{x-1} \tag{3}$$

$$\hat{y}_{x+1} = l_x + b_x \tag{4}$$

$l_x$  represents the intercept.  $y_x$  represents the current value of the sequence.  $b_x$  indicates the slope (or trend).  $\beta$  the coefficient represents the weight of exponential smoothing.  $\hat{y}_{x+1}$  represents the predicted value of the last series.

When the curve has a trend change, triple-exponential smoothing is often used for analysis [28]. The triple-exponential smoothing method principle formula is as follows:

$$l_x = \alpha(y_x - s_{x-l}) + (1 - \alpha)(l_{x-1} + b_{x-1}) \tag{5}$$

$$b_x = \beta(l_x - l_{x-1}) + (1 - \beta)b_{x-1} \tag{6}$$

$$s_x = \gamma(y_x - l_x) + (1 - \gamma)s_{x-l} \tag{7}$$

$$\hat{y}_{x+m} = l_x + mb_x + s_{x-l+1+(m-1)modl} \tag{8}$$

$l_x, y_x, b_x, \beta$  here have the same meaning as above.  $s_x$  represents seasonal components.  $\gamma$  the coefficient represents the weight of exponential smoothing.  $\hat{y}_{x+m}$  indicates the predicted value after the next  $m$  steps.

The Brutlag method is also introduced in the triple-exponential smoothing model to create a confidence interval:

$$\hat{y}_{\max_x} = l_{x-1} + b_{x-1} + s_{x-T} + m \cdot d_{t-T} \tag{9}$$

$$\hat{y}_{\min_x} = l_{x-1} + b_{x-1} + s_{x-T} - m \cdot d_{t-T} \tag{10}$$

$$d_t = \gamma|y_t - \hat{y}_t| + (1 - \gamma)d_{t-T} \tag{11}$$

where  $T$  is the length of the season and  $d$  is the forecast deviation. The value of alpha is the key to determining the final result in the exponential smoothing analysis [29]. The value of  $\alpha$  ranges from 0 to 1. According to experience, it is usually within the range of 0.10 to 0.90 [30].

### 2.2.2. Correlation Analysis

In meteorological data research, to understand the relationship between the research object and other factors, the correlation is used to measure the closeness of the relationship between two random variables [31–33]. If the absolute value of the correlation coefficient is large, the relationship is considered to be close, otherwise the relationship is considered not to be close. At the same time, whether the calculated correlation coefficient is significant needs to pass the significance test. In this paper, the correlation analysis method is used to explore the relationship between OLR data and TCWV, AT, CTP, and CTT; and conduct a significance test on the results, and finally get relevant conclusions. The principle formula is as follows:

$$r = \frac{\frac{1}{n} \sum_{i=1}^n (x_i - \bar{x})(y_i - \bar{y})}{\sqrt{\frac{1}{n} \sum_{i=1}^n (x_i - \bar{x})^2} \sqrt{\frac{1}{n} \sum_{i=1}^n (y_i - \bar{y})^2}} = \frac{\text{cov}(x, y)}{S_x S_y} \quad (12)$$

### 2.2.3. Empirical Orthogonal Function

The EOF decomposition can separate the time and space changes of the element field, decompose the time-varying element field into the sum of the products of the time-invariant spatial function and the time-dependent time function, and use as few modes as possible express to the main time and space changes [34,35]; to objectively and quantitatively reflect the spatial structure and time changes of the element field, which has been widely used in the research of atmospheric science [36].

## 3. Spatiotemporal Variation Characteristics Analysis

### 3.1. Spatial Variation Analysis

#### 3.1.1. Year-By-Year Spatial Distribution of OLR in the Past 19 Years and 19-Year Average

Figure 1 shows the year-by-year spatial distribution of OLR in the past 19 years and the 19-year average. It can be seen from Figure 1 that the changing trend in the entire East Asia region is not obvious, indicating that the annual average change of OLR in the East Asia region in the past 19 years is small. However, the spatial trend of OLR in East Asia at 10–30° N latitude has always been a high-value area year-by-year, while it has always been a low-value area at 50–60° N latitude, indicating that the OLR value decreases with the increase of latitude. It can also be seen from Figure 1 that in addition to the low-value area of 50–60° N, another area with a low value is the Qinghai-Tibet Plateau, which is due to the complexity of its terrain and climate. In the meantime, we can know from local observations that the size of the OLR value in the entire Chinese region remains basically unchanged. However, it can be found that the annual spatial OLR variation has a certain increase or decrease in East Asia, and is mainly reflected in some waters of the Western Pacific Ocean and Indian region. This result may be due to the influence of the western Pacific subtropical high on solar radiation, which makes the near-surface atmosphere gain more heat, the atmospheric temperature rises or decrease significantly, and the OLR value change significantly. The Indian region may be due to its tropical monsoon climate, high temperature all year round, and the obvious distribution of precipitation and dry season. Therefore, the year-by-year change of OLR value is related to temperature and seasonal precipitation.

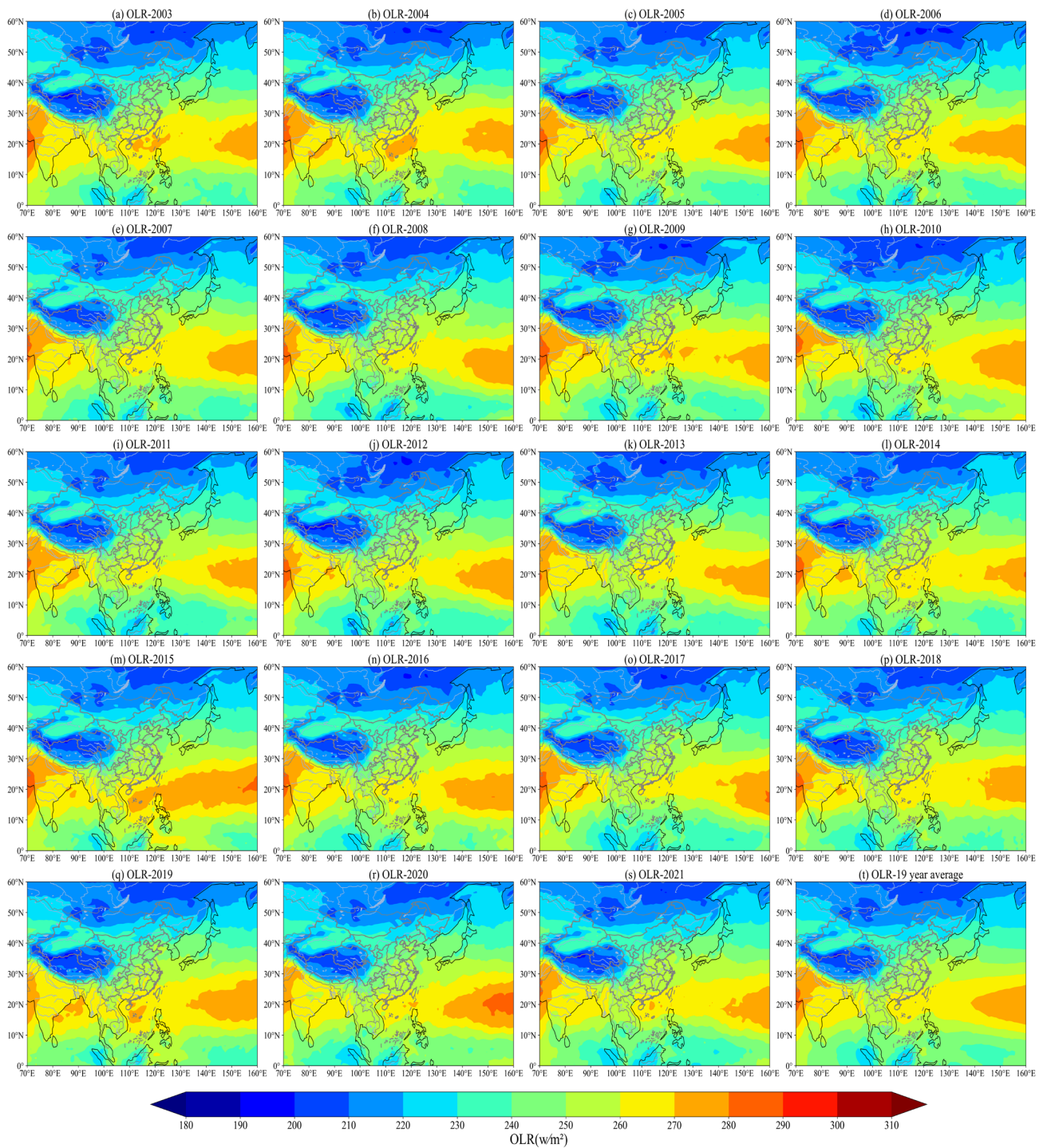


**Figure 1.** Year-by-year spatial distribution of OLR in East Asia in the past 19 years and the 19 year average.

### 3.1.2. Seasonal Spatial Variation Distribution of OLR in the Past 19 Years

Figure 2 shows the seasonal spatial variation distribution of OLR in the past 19 years. From the latitude distribution, it can be found that the variation of OLR gradually increases with the decreases in latitude, which is similar to the relationship between the spatial distribution and latitude of OLR year by year. However, the OLR value in the range of  $0\sim 10^\circ N$  is higher than that of  $40\sim 60^\circ N$  and lower than that of  $10\sim 30^\circ N$ . It may be because  $0\sim 10^\circ N$  is close to the equator, and the cloudiness near the equator is more [37], which shields the propagation of part of the OLR value, resulting in the OLR value near

the equator being lower than 10~30° N and higher than 40~60° N. From Figure 2, It can also be found that the OLR value in other parts of East Asia is much higher than that of the Qinghai-Tibet Plateau. As the third pole other than the North and South Poles, the Qinghai-Tibet Plateau has a higher altitude, a complex terrain environment, and a higher atmospheric temperature. The OLR value of other parts of East Asia is higher than that of the Qinghai-Tibet Plateau. OLR values were found to be lower in spring and winter than in summer and autumn, with summer being the highest of the year, followed by autumn, which may be because of the influence of temperature and cloud cover. Because the higher the temperature, the stronger the radiation ability of OLR, and the higher the cloud cover, the weaker the radiation ability. So, the OLR distribution in summer is higher than in other seasons. In addition, through the spatial distribution of the four seasons, it is found that the high-value areas in summer are in Beijing-Tianjin-Hebei, Shandong, Henan, northern Anhui, and the western Pacific Ocean and India, In China, while the high-value areas in autumn have moved southward for summer, making its high-value areas in Guangxi, Guangdong, Fujian, and other places, the high OLR areas in winter are in the western Pacific Ocean and the Bay of Bengal, and are much higher than in other seasons. At the same time, we see that the OLR value in South Asia is also relatively high, which may be due to the warming of the temperature in South Asia, resulting in a higher surface temperature and affecting the change of OLR [38].

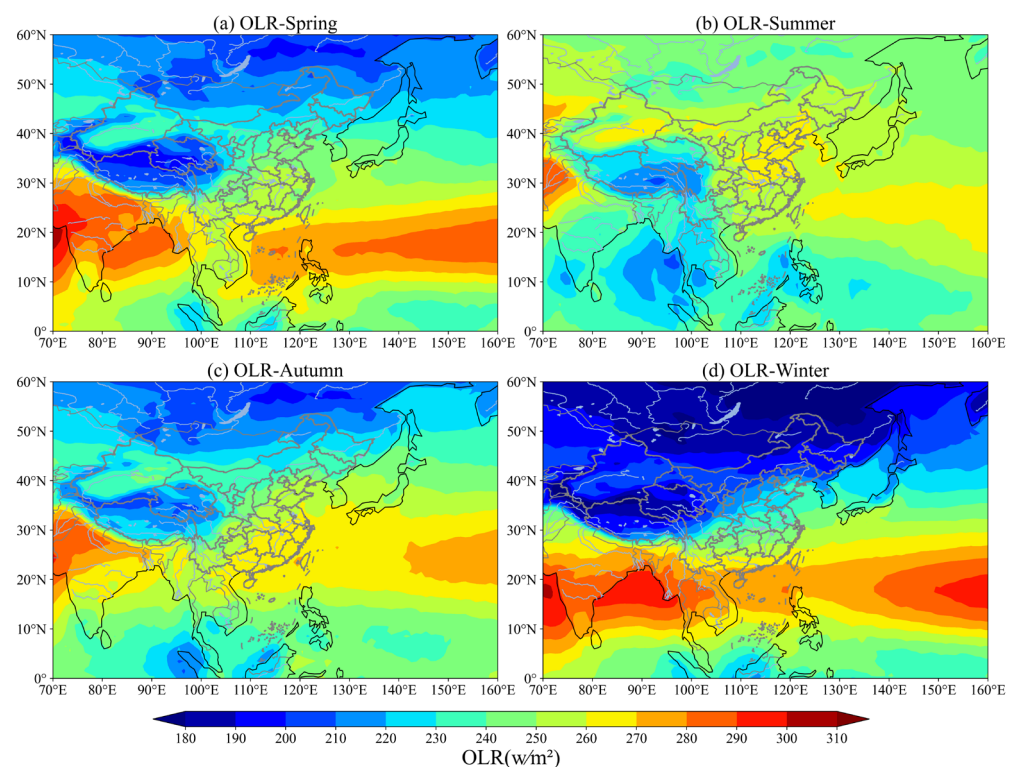


**Figure 2.** Seasonal spatial variation distribution of OLR in East Asia in the past 19 years.

### 3.1.3. Average Monthly Spatial Distribution of OLR in the Past 19 Years

As shown in Figure 3, it is found that the OLR spatial distribution in May–October is higher than in other months. The possible reason is that from May to October, including summer, the end of spring and the beginning of autumn, the temperature is relatively higher, making the OLR at a high value. This may indicate that the OLR spatial distribution in East Asia has a great correlation with air temperature. Although the OLR value from May to October is higher than in other months, the division of high and low-value areas is not obvious, while in other months, the high- and low-value areas are at 10~30° N and 40~60° N, which means that in other months, the OLR value obviously decreases with the increase in latitude. According to the division of the natural year, it can be found from

Figure 3 that OLR in spring and autumn has remained basically unchanged in East Asia. In summer, the range of 10–30° N latitude gradually decreases and the range of high-value areas gradually decreases, while other latitudes gradually increase, while the change in 10–30° N latitude in winter is just opposite to that in summer. This is most likely because the latitude range of 10~30° N is close to the equator, and the cloudiness near the equator obscures the propagation of OLR. At the same time, we know that a higher temperature causes higher water vapor and higher cloudiness, and a lower temperature, less water vapor and less cloudiness. This leads to opposite trends in summer and winter.

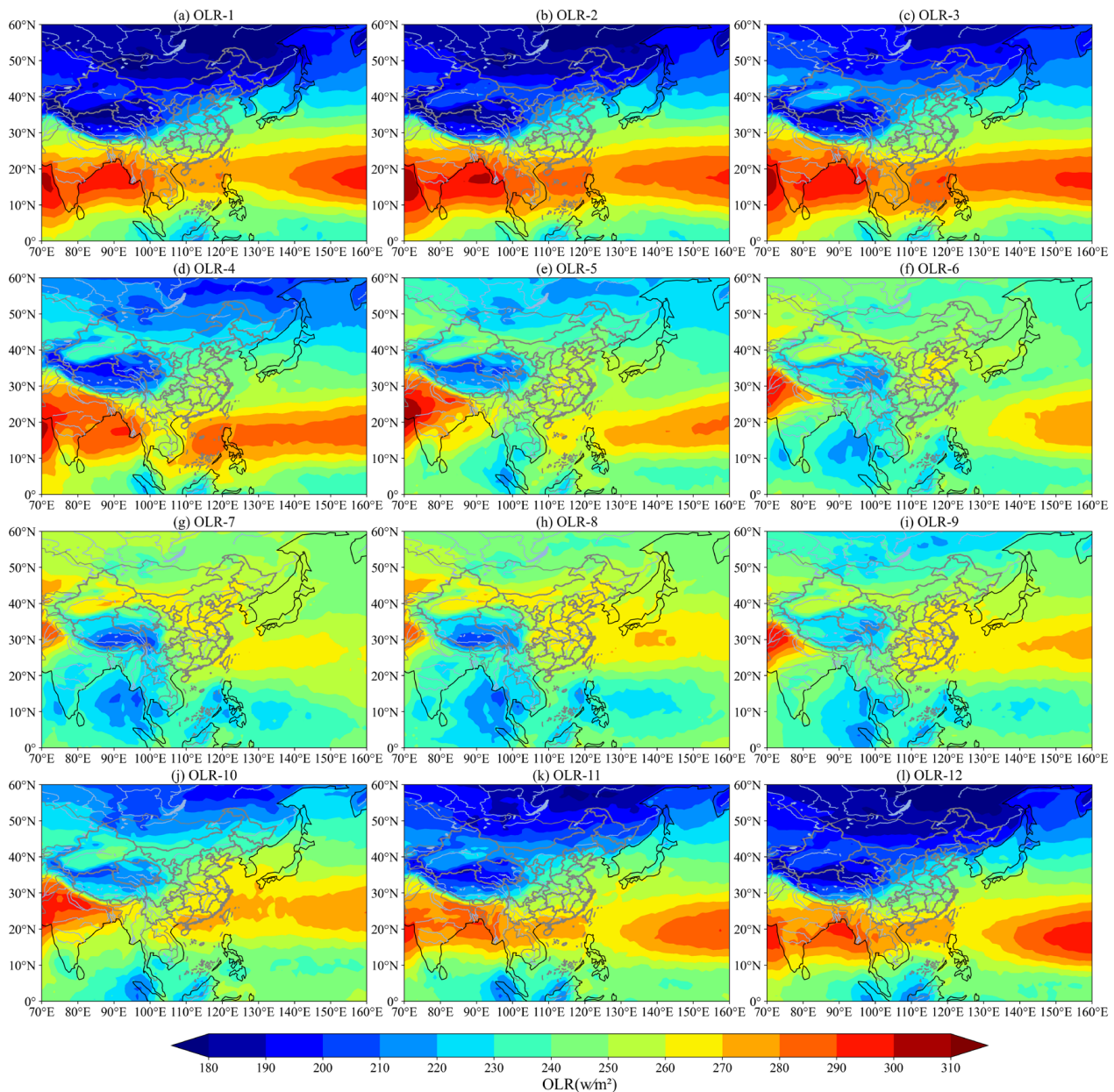


**Figure 3.** Average monthly spatial distribution of OLR in East Asia in the past 19 years.

### 3.2. Time Evolution Analysis

#### 3.2.1. OLR Multi-Dimensional and Multi-Angle Analysis

Figure 4a shows the OLR time series changes at the same longitude and different latitudes. From Figure 4a, it can be known that the OLR value at 10–30° N latitude is higher than at other latitudes. Except for 0–10° N latitude, other latitudes with the decreases of latitude and the OLR value gradually increase. This is because the latitude of 0~10° N

is close to the equator and the cloudiness near the equator is higher, which obscures the propagation of part of the OLR. As a result, it corresponded well to the spatial distribution. Figure 4b shows the year time and latitude changes. It can be found that the inter-annual changes in Figure 4a, b have a similar trend. Meanwhile, it is found that 2015 is the highest value year in the past 19 years, which may be the reason this is the result of the longest El Niño “Bruce Lee” in 2015 and the warmest year on record. Figure 4c shows the inter-annual change in OLR in East Asia. Figure 4c, it is found that 2015 is the high point of inter-annual change of OLR, which corresponds to the results in Figure 4b, and the change rate in the past 19 years is  $0.04 \text{ w/m}^2$  per year. The OLR reached its lowest value in 2012, with a value of about  $238 \text{ w/m}^2$ . This may be because the La Nina extreme low-temperature event that ended at the beginning of 2012 has a certain cooling effect on the world, resulting in the lowest OLR value in history in 2012. Figure 4d shows the monthly time and latitude changes. It can be found from Figure 4d that the OLR value is the lowest in July at the latitude of  $10\sim 30^\circ \text{ N}$ . At the same time, the months on both sides gradually increased, and high-value areas appeared in January, February, March, and December, which were similar to the spatial distribution characteristics. The changed trend of OLR between  $30\sim 60^\circ \text{ N}$  and  $10\sim 30^\circ \text{ N}$  is the opposite. July is the highest value of the OLR value and decreases on both sides of the month, with low-value areas appearing in January, February, and December.

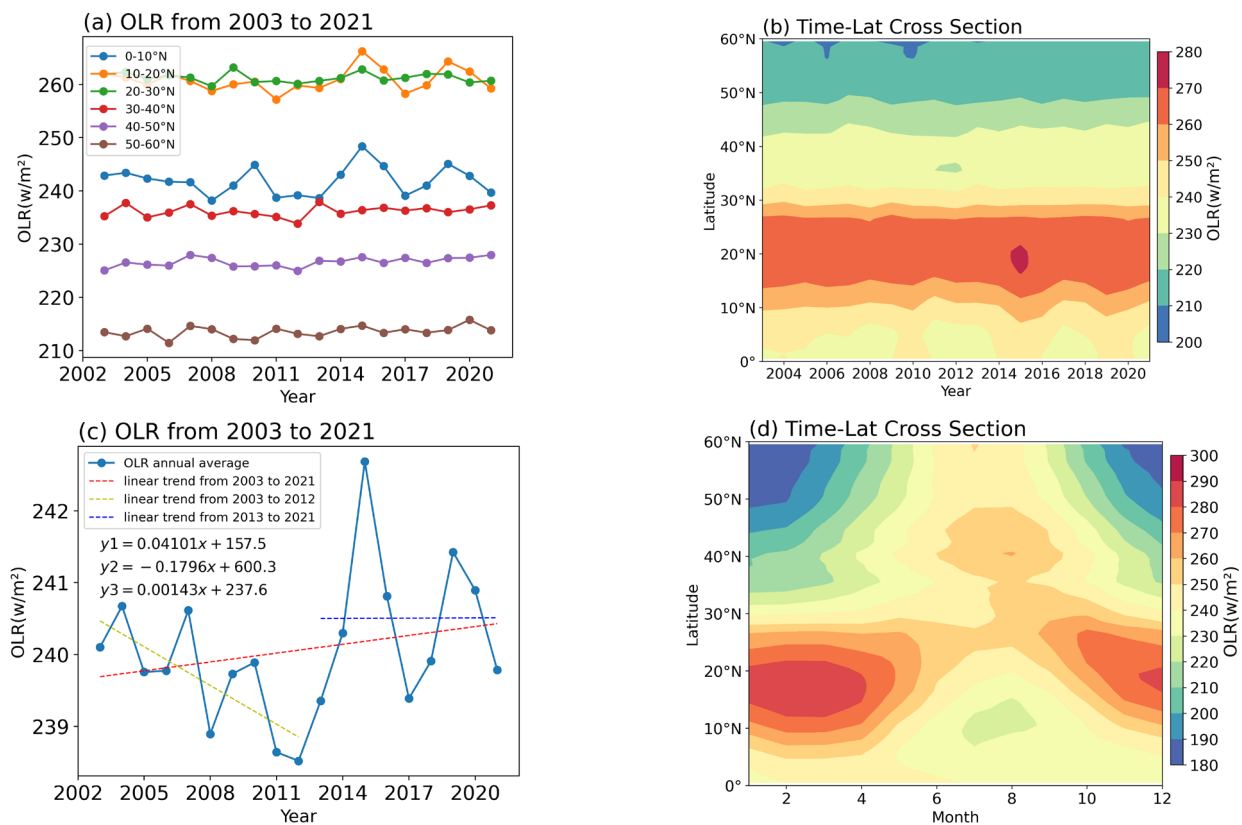


**Figure 4.** OLR multi-dimensional and multi-angle analysis. (a) Time-series changes of the same longitude and different latitudes. (b) Year time and latitude changes. (c) Time-series changes in special areas. (d) Monthly time and latitude changes.

### 3.2.2. Exponential Smoothing Analysis

Figure 5a shows the single-exponential smoothing results. From Figure 5a, it can be seen that the actual monthly data change of OLR is the light-blue line, while the orange and dark-blue lines represent results obtained when different  $\alpha$  values are taken. We found that when  $\alpha = 0.2$ , the time-series change value of OLR has a large error compared with the actual value, which indicates that the test value cannot keep up with the change trend



of the actual value and the fluctuation is relatively small; so, the time-series comparison is smooth. When  $\alpha = 0.8$ , the test result can be close to the true value. However, the obtained  $\alpha$  value is relatively large, indicating that the real-time sequence has a strong trend change and this method cannot be used for prediction. Figure 5b is the result of the double-exponential smoothing method. Based on the single-exponential smoothing method, an additional  $\beta$  value is added, compared with the single-exponential smoothing method that only considers the previous  $K$  historical data and static values. The double-exponential smoothing method “averages” historical data and also takes into account the upward trend of current data changes, which is the result of the interaction between  $\alpha$  and  $\beta$ . From Figure 5b, it can be known that the purple line is the actual OLR change. The rest are the time series that approximates the actual value obtained under the action of different  $\alpha$  and  $\beta$ . When  $\alpha = 0.9$  and  $\beta = 0.02$ , it can better approach the change of the actual value; and the deviation of  $\alpha = 0.02$  and  $\beta = 0.02$  from the actual value is the most obvious. At the same time, under the action of the same  $\alpha$  and different  $\beta$ , if  $\alpha$  is small, no matter how large  $\beta$  is, it cannot be very close to the actual value. When  $\alpha$  is large, no matter what value  $\beta$  takes, it can better fit the actual value. Meanwhile, the  $\beta$  value is smaller, the closer it is to the actual value, indicating that  $\alpha$  occupies the main influence on the double-exponential smoothing method. Therefore, in order to get the result closer to the actual value, you can set  $\alpha$  to be larger and  $\beta$  to be smaller; otherwise, it will not fit well.

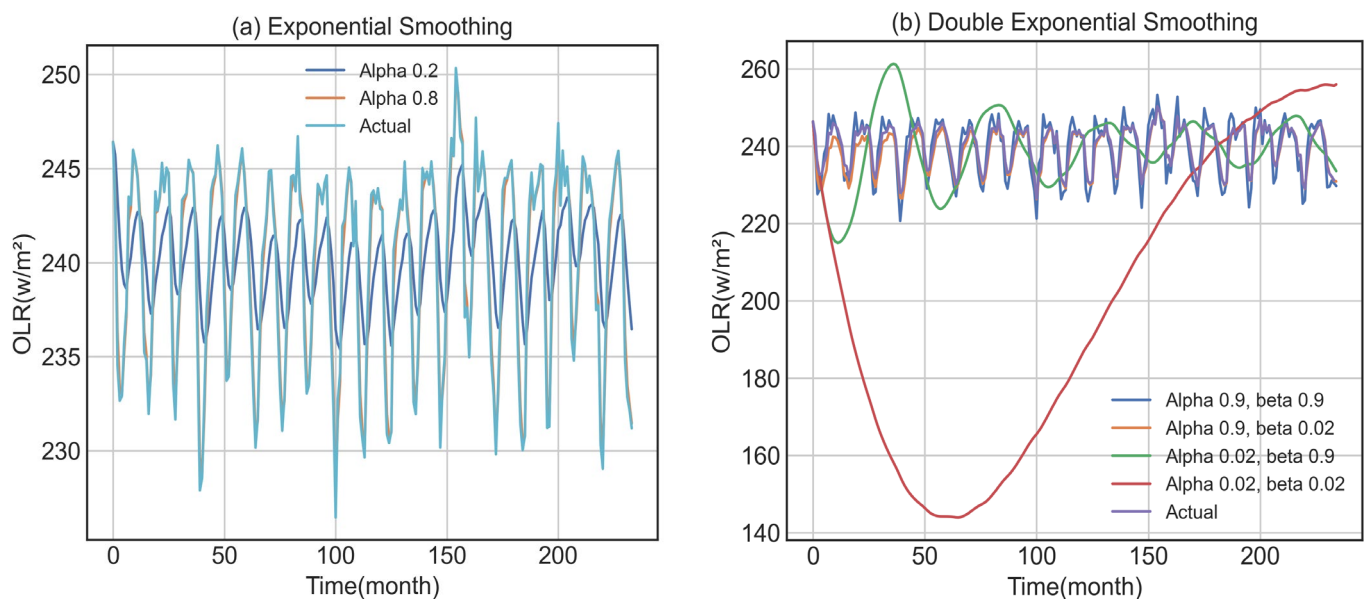


**Figure 5.** Exponential smoothing analysis: (a) exponential smoothing and (b) double-exponential smoothing.

### 3.2.3. Triple-Exponential Smoothing Analysis and Prediction

Figure 6a shows the prediction results of the triple-exponential smoothing. The triple-exponential smoothing adds a seasonal trend analysis to the double-exponential smoothing; in addition, the seasonality is used to explain the repeated changes of the intercept and trend, and is described by the length of the season. In this article, we take the seasonal step size as 24. It can be seen from Figure 6a that both the actual value and the predicted value can satisfy the confidence interval. In addition, it is found that the prediction model results and the actual value results can be well fitted to approach the initial time series and capture seasonality. However, the overall downward trend has some anomalies. At the same time, the green dots are the unstable point in the whole time series. There are two outliers in the figure: one appears in the initial stage of the OLR time series and the other anomaly occurs at the end of the actual time series, indicating that in the prediction process, there will be interference at the beginning; and when it gradually stabilizes, the outliers will be

such that it does not appear. Moreover, the time series will be affected by the white noise of the system and the results of human operation during the acquisition of atmospheric data factors when it is about to end. At the same time, from the model deviation diagram in Figure 6b, it can be found that the model responds very strongly to changes in the sequence structure at the beginning. However, the deviation will soon return to the normal value and “forget” the past, which indicates that the model has no memory function; in addition, the range of deviation is mainly between 0.5 and 2.5, and the deviation is small. Furthermore, from the prediction results in Figure 6a, it is found that the accuracy is higher and the error is smaller. The prediction results have a certain reference, indicating that the results can provide a reference value for future data research.

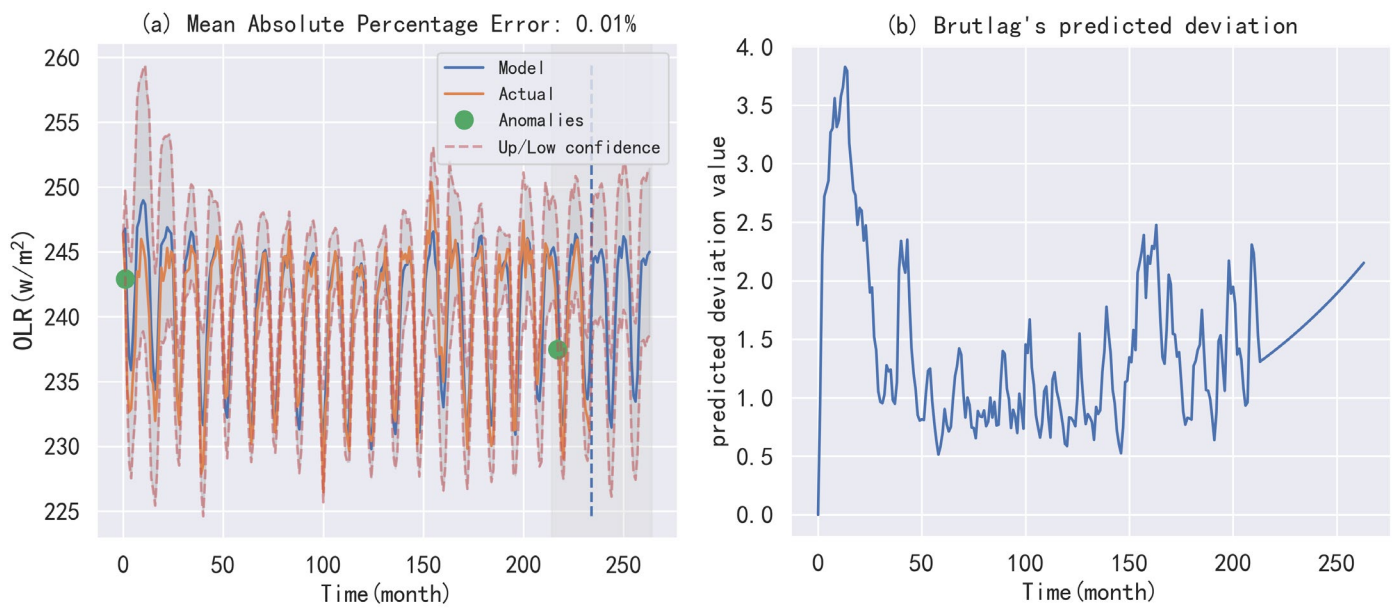


**Figure 6.** Triple-exponential smoothing analysis and prediction: (a) triple-exponential smoothing prediction results and (b) predicted deviation.

### 3.3. Empirical Orthogonal Decomposition (EOF)

The OLR data of 19 years from 2003 to 2021 are anomaly model analysis. Then, the datasets are decomposed by EOF, and the time-invariant spatial function and time-varying time function of the 19-year East Asian region are obtained. In a physical sense, the greater the variance contribution of the decomposed spatial function, the better the understanding of the spatial variation characteristics of OLR in the past 19 years. Meanwhile, the time function can reflect whether the annual contribution is decreasing or increasing, and obtain the overall change trend of 19 years and the changing trend of each decade.

Four eigenvectors and four-time coefficients are obtained through EOF decomposition, as shown in Table 1.

**Table 1.** The first four EOF of the variance contribution and cumulative variance (unit: %).

Mode	EOF1	EOF2	EOF3	EOF4
Variance contribution	43.29%	16.72%	5.22%	4.94%
Cumulative variance	43.29%	60.01%	65.23%	70.17%

The trend lines of the time coefficient in the past 19 years, 2003~2012 linear trend lines, and 2013~2021 linear trend lines to make a table are shown in Table 2.

**Table 2.** The overall trend line of PC value in 19 years and the trend line of each decade.

PC	2003~2021 Linear Trend	2003~2012 Linear Trend	2013~2021 Linear Trend
PC1	$y = -0.01222x + 24.58$	$y = 0.1891x - 379.3$	$y = 0.03597x - 72.84$
PC2	$y = -0.06419x + 129.2$	$y = -0.208x + 417.7$	$y = -0.04182x + 84.16$
PC3	$y = -0.03616x + 72.76$	$y = 0.08142x - 163.3$	$y = -0.1645x + 331.7$
PC4	$y = -0.07497x + 150.8$	$y = 0.1014x - 203.1$	$y = -0.1257x + 253.1$

It can be found in Table 1 that the OLR value after EOF decomposition has a fast convergence speed, and the total modal variance contribution after decomposition exceeds 70%. The main information of the anomaly field is concentrated, which has high research significance. The variance contribution of EOF1 (Figure 7a) and EOF2 (Figure 7c) in Table 1 is much higher than that of the other two modes; so, only the first two modes with high contribution are analyzed here, and the latter two modes are analyzed similarly to the first two modal analyses. From Figure 7a, it can be seen from EOF1 that it is negative in the range of 0~25° N in East Asia, and has extremely low negative values in the range of 100~135° E, while Sichuan, Chongqing, and western parts of the Pacific Ocean are positive. At the same time, combined with the time coefficient principal component (PC)1 (Figure 7b), it can be found that the overall change trend of PC1 is a downward trend, indicating that the value of OLR in the range of 0~25° N and 100~135° E in East Asia shows an upward trend; and Sichuan, Chongqing, and parts of the western Pacific are on a downward trend. From Table 2, it can be seen that the time trend of the first 10 years and the last 9 years is an increase, indicating that the total OLR value decreased more than increased during the 19 years. It can be seen from EOF2 (Figure 7c) that positive values are found in South China, Southwest China, Taiwan, East China Sea, Southeast Asia, the Bay of Bengal, and South India; and extremely high-value areas appear in Guangdong, Fujian. However, the region of Northwest China, the Qinghai-Tibet Plateau, and some waters of the western Pacific showed negative values; and the negative values were more obvious in some waters of the western Pacific. At the same time, combined with the change of the time coefficient PC2 (Figure 7d), it is found that there is a downward trend in 19 years, indicating that the OLR values in Southwest China, Taiwan, the East China Sea, Southeast Asia, and the Bay of Bengal have a decreasing trend. Moreover, northwest China, the Qinghai-Tibet Plateau, and parts of the western Pacific Ocean show an increasing trend. From Table 2, we can find that the changing trend of the first 10 years and the last 9 years is also decreasing, which shows that the changes of the first 10 years and the last 9 years are the same as the changes of the whole 19 years. At the same time, it can be seen through PC2 that the first 5 years are all positive, indicating that the change in the first 5 years is the opposite of the overall change in the first 10 years and the last 9 years. In addition, after 2008, the time coefficient is a negative value and reduced the amount of OLR more than in the previous 5 years, ultimately leading to a downward trend in the change over 19 years.

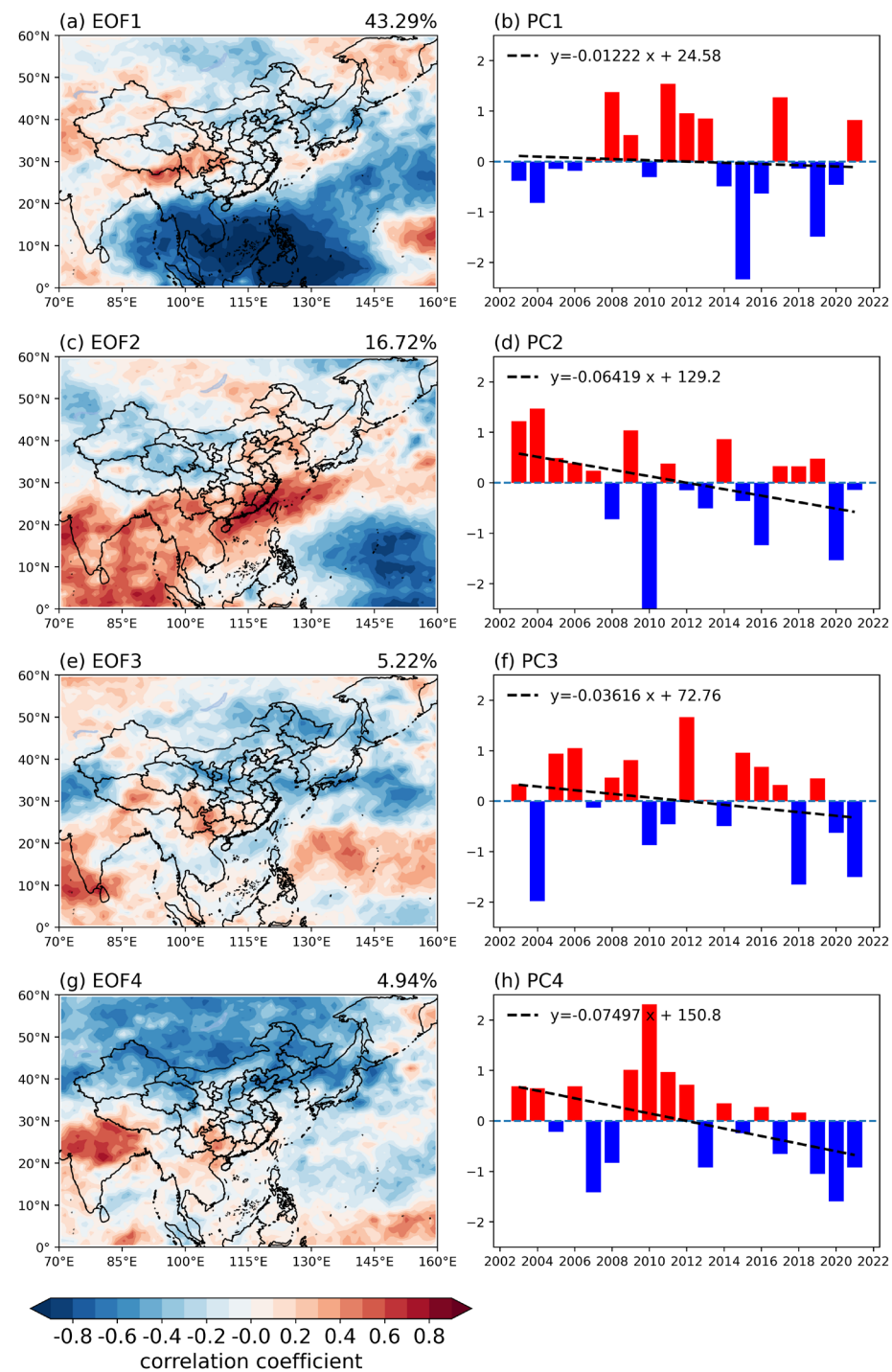


**Figure 7.** The result of empirical orthogonal decomposition in East Asia.

#### 4. Relationship between OLR and TCWV, AT, CTP, and CTT

##### 4.1. Spatiotemporal Characteristics Analysis of TCWV, AT, CTP, and CTT

Figure 8a,c,e,g shows the multi-year spatial distribution of TCWV, AT, CTP, and CTT. Figure 8b,d,f,h for the inter-annual variation. From the spatial distribution of Figure 8a,c, it can be found that the spatial distribution of TCWV and AT are basically the same. It is in the high-value area between 0 and 25° N, and mostly in the ocean area, while the lower-value area is located in the Qinghai–Tibet Plateau. From the spatial distribution of CTP and CTT in Figure 8e,g, it can be seen that the high-value areas of CTP appear in northeastern China, South Korea, and North Korea; and the low-value area is in the range of 0~10° N. At the same time, it can be found that the Qinghai-Tibet Plateau is the lower-value area

in the whole of China, and the spatial distribution of CTT and CTP is relatively similar; but, the high-value area of CTT is in India and the CTP is different. Figure 8b shows the inter-annual variation of TCWV. It can be seen that the inter-annual variation of TCWV shows an upward trend, and it also increases with different slopes in the first ten years and the next nine years; but, there is a downward trend in the process of increasing from 2010 to 2015. This may be caused by the upward trend of OLR during this period. Figure 8d shows the inter-annual variation of AT. This trend is similar to the variation trend of TCWV, both of which are increasing, and there is also a decreasing trend from 2007 to 2012. At the same time, among the inter-annual changes in the past 19 years, it reached the maximum value in 2020. It can be seen from Figure 8f,h that CTP and CTT have similar changing trends. However, the overall trend of CTP is decreasing, and the trend of CTT is increasing. In addition, the changing trend in the next nine years is also the opposite. At the same time, both reached the lowest values in 2008, which were 515 hpa and 251 °C.

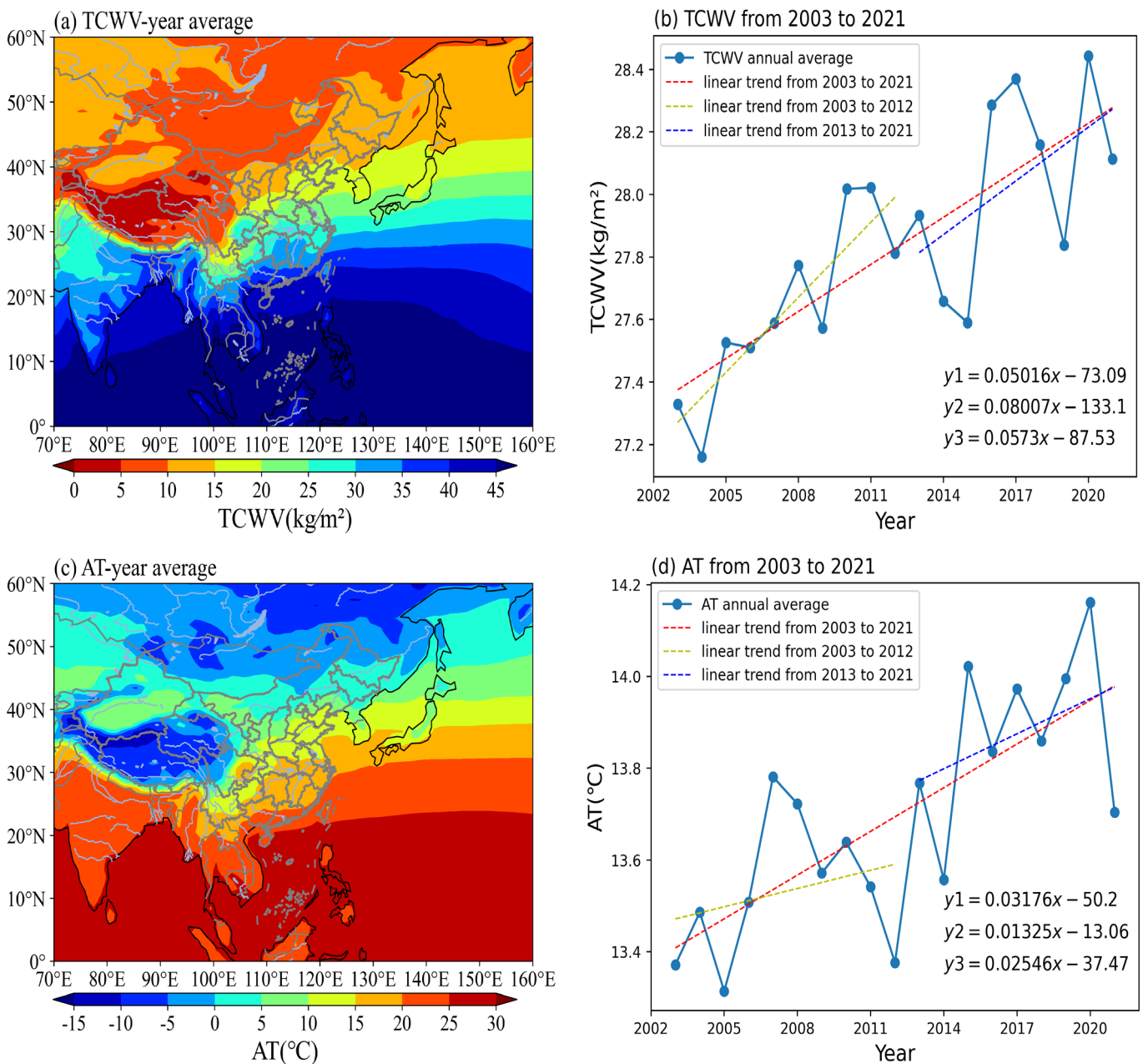
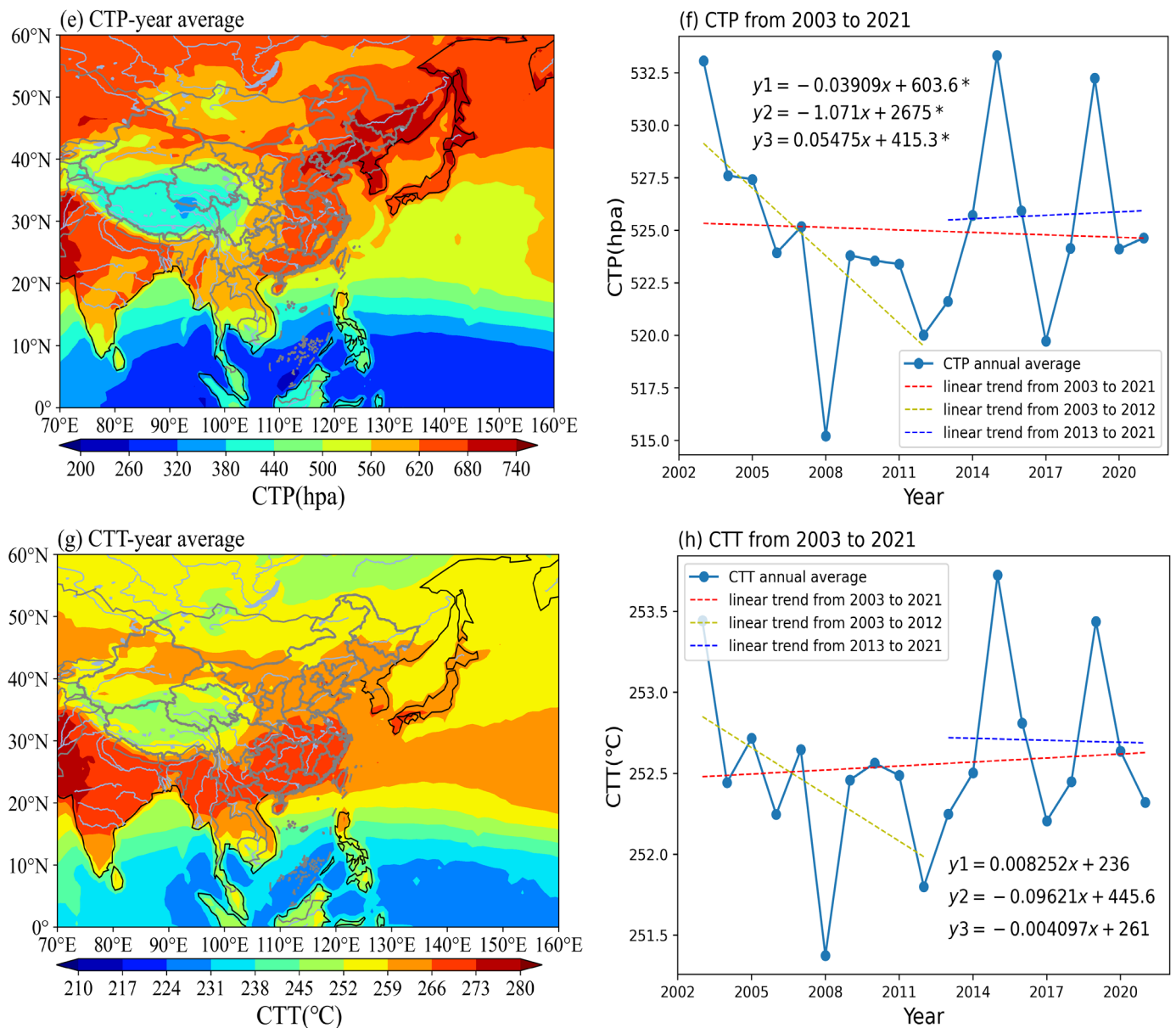


Figure 8. Cont.



**Figure 8.** The parameters of (a,c,e,g) are spatial distribution, and the parameters of (b,d,f,h) are time variation.

4.2. The Correlation between OLR and Impact Factors

Figure 9 shows the results of the correlation study between the OLR data detected by AIRS, and the monthly data of TCWV, AT, CTP, and CTT. In Figure 9, N = 234 is the number of datasets. From the results shown in the figure, it can be known that Figure 9a,b,d are the correlations between OLR and TCWV, AT, and CTT. It is found that the correlation between OLR and these three factors appears to be positively correlated. At the same time, the correlation between OLR and AT is the largest at 0.89, while the correlation with TCWV and CTT is smaller at 0.78. However, the correlation between OLR and these three factors exceeds the limit of strong correlation (weak correlation is 0~0.3, medium correlation is 0.3~0.6, a strong correlation is 0.6~1), indicating that between the OLR and these three parameters has a very strong positive correlation; so, the OLR value may gradually increase with the increase in TCWV, AT, and CTT. We can also find that the slope of the fitted straight line between OLR and CTT is the largest among the three, indicating that OLR is greatly affected by CTT. At the same time, the correlation coefficients of the three have passed the 99% significance t-test. In Figure 9c, it can be seen that the correlation coefficient between

OLR and CTP is  $-0.64$ , indicating that OLR and CTP have a strong negative correlation, indicating that the OLR value may gradually decrease with the increase of CTP. In addition, its absolute slope is the smallest among the four graphs, and its correlation coefficient also passed the 99% significance test. However, only a linear correlation can be seen here. In the following subsections, we will analyze its correlation in East Asia in detail, so that we can more intuitively see the size of the correlation in various places in East Asia, which is convenient for future research by scholars.

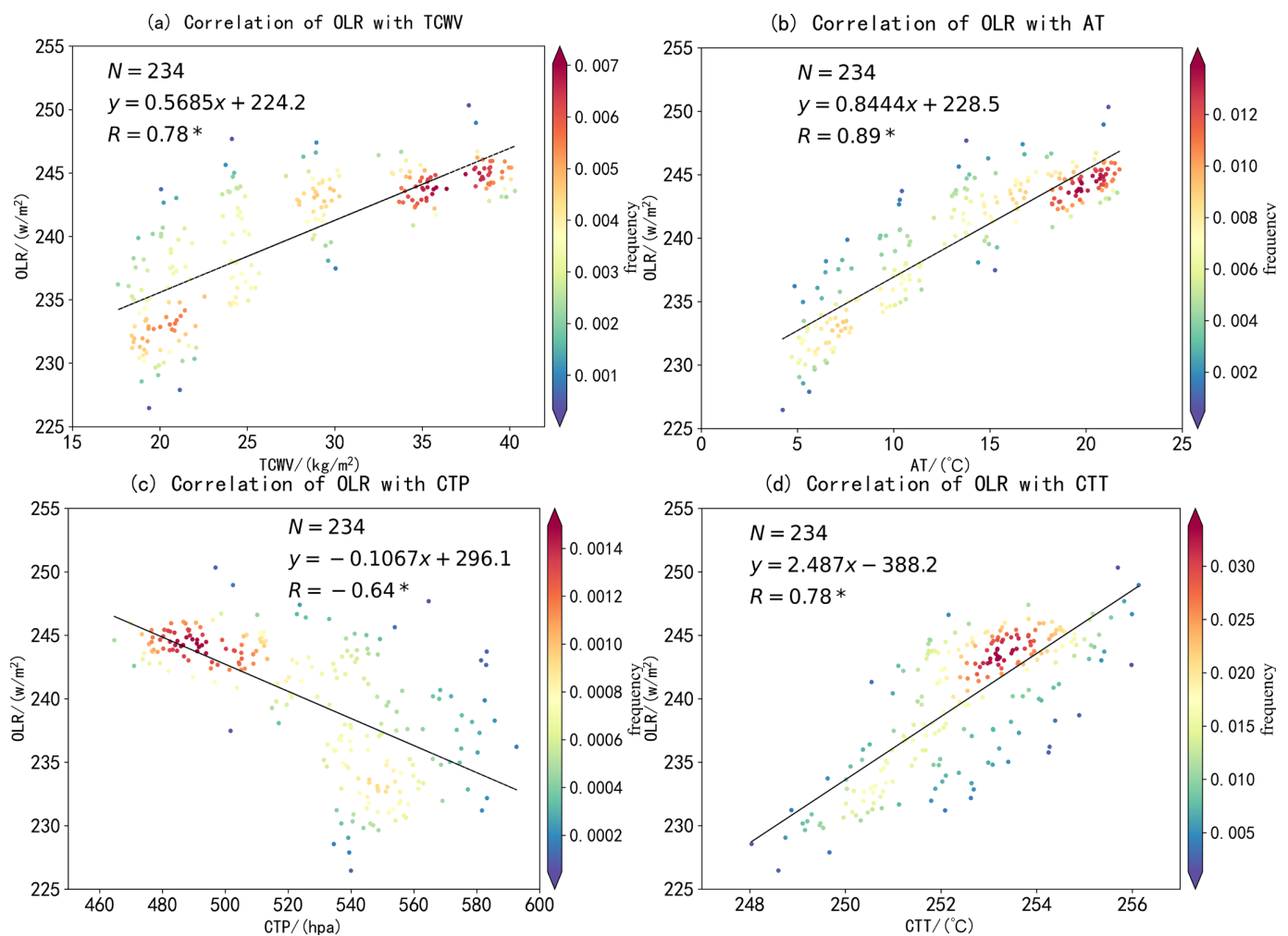


**Figure 9.** The correlation between OLR and various factors. \* Indicates passing the 99% significance test. (a) OLR and TCWV. (b) OLR and AT. (c) OLR and CTP. (d) OLR and CTT.

#### 4.3. The Longitude–Latitude Distributions of Correlation between OLR and Impact Factors

Figure 10 represents the longitude-latitude distributions of the spatial correlation and significance test between OLR and influencing factors. Figure 10a is the spatial correlation between OLR and TCWV. From Figure 10a, it can be seen that there is a positive correlation between  $30$  and  $60^{\circ}$  N. The correlation degree is above  $0.8$ . At the same time, the negative correlation degree is above  $0.8$  in most places from  $0$  to  $25^{\circ}$  N, and these places passed the 99% significance test. It shows that the OLR may increase with the rise of the TCWV at  $30\sim 60^{\circ}$  N, and the opposite is true at  $0\sim 25^{\circ}$  N. In addition, a relatively obvious dividing line can be seen in the range of  $25\sim 30^{\circ}$  N, which distinguishes between a high positive correlation and negative correlation. It can be seen from Figure 10b that the spatial correlation of AT is basically the same as that of Figure 10a, except that the positive correlation between AT and OLR is higher above  $30^{\circ}$  N; while the negative correlation below  $20^{\circ}$  N is the same as that in Figure 10a, the correlation between AT and OLR becomes

lower. Figure 10c is a schematic diagram of the correlation between OLR and CTP. From the distribution in the figure, it can be seen that the spatial correlation between CTP and OLR, the correlation between TCWV and OLR, and AT and OLR basically show opposite trends. In South Korea, North Korea, Japan, and northern China, the correlation is basically negative; and the correlation is mostly positive in other regions. Moreover, in Southeast Asia and southern India, the positive correlation is abnormally high, as high as 0.9 or more. Figure 10d shows the spatial correlation between OLR and CTT. It can be found that there is a positive correlation of more than 0.8 in most parts of East Asia, and only a few areas have a low negative correlation and a very low correlation, such as in the East China Sea waters of China, parts of southern Japan, and parts of eastern Indonesia; there is only a correlation of no more than 0.5. In addition, we can find that OLR and CTT in East Asia basically pass the 99% significance test, indicating that OLR variation is highly influenced by CTT throughout East Asia. The analysis of the above results shows that the positive correlation at 30° N to 60° N in East Asia is mainly affected by the TCWV, AT, and CTT; and the negative correlation is greatly affected by CTP. The positive correlation between 0 and 25° N is affected by CTP and CTT, and the negative correlation is affected by TCWV and AT.

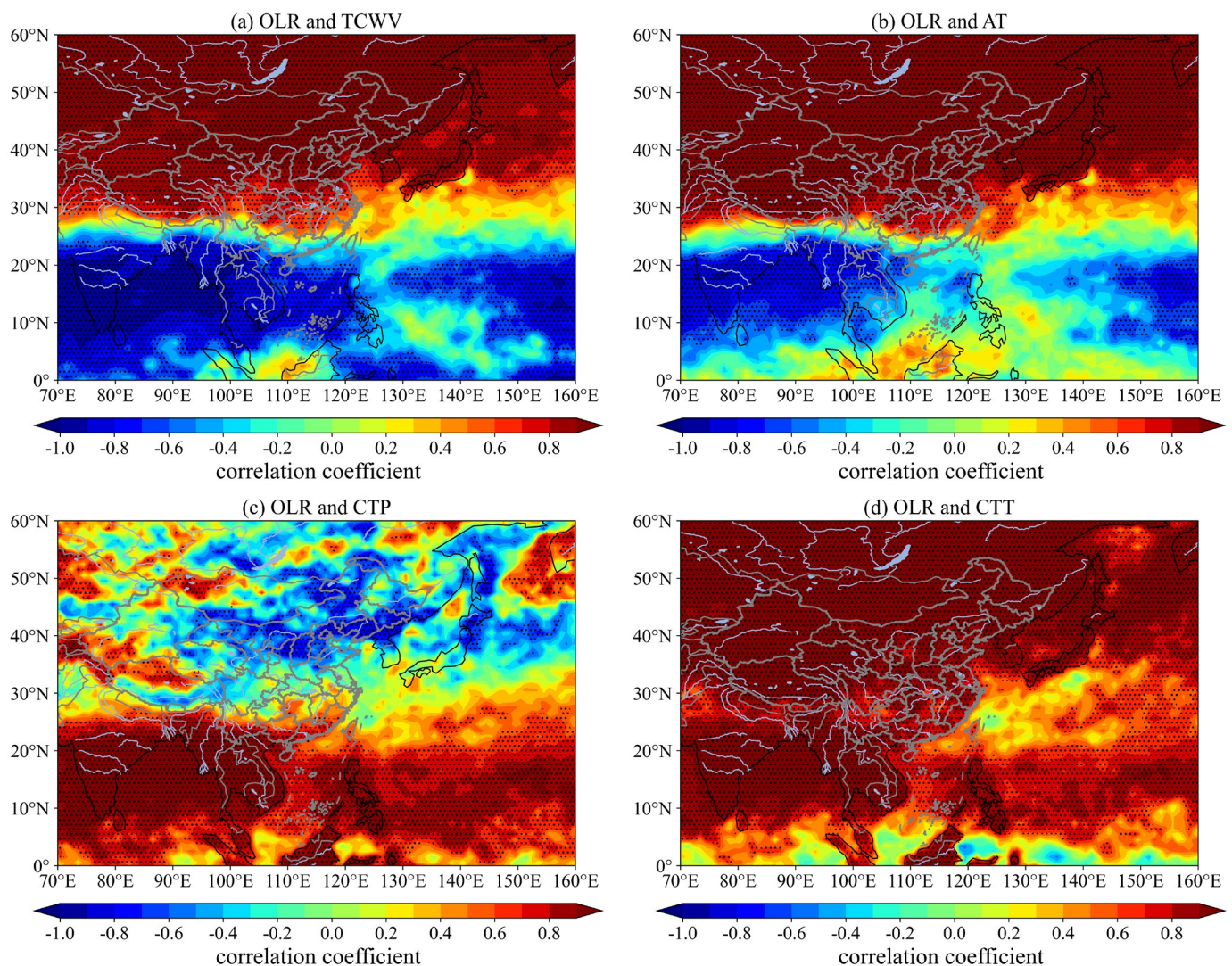


**Figure 10.** The longitude–latitude distributions of correlation between OLR and various factors; the black dots indicate that they passed the 99% significance test. (a) OLR and TCWV. (b) OLR and AT. (c) OLR and CTP. (d) OLR and CTT.



## 5. Discussion

This paper uses AIRS remote-sensing OLR data for 19 years from 2002 to 2021 to analyze its temporal and spatial, modal, and correlation results. Firstly, from analysis of the OLR temporal and spatial variation, we understand its spatial distribution and temporal changes in East Asia. At the same time, we study the correlation between OLR and some factors. The changes in OLR and the results of correlation research provide help in studying some extreme weather.

Among some outstanding foreign researchers, there are sixth-time series prediction models used to detect OLR anomalies before and after earthquakes; then, a new forecasting method improved based on the ARIMA forecasting model is proposed for forecasting [39]. Some researchers have studied the potential of abnormal changes in OLR in earthquake precursors [40]. Other researchers used the background field analysis (BFA) method and tidal force pulsation analysis method to obtain OLR data separately to study whether OLR data is the main factor causing seismic tectonic force [41]. It can be seen that most of them are based on earthquakes to study the abnormal changes of OLR. However, this paper conducts research by directly analyzing the OLR data observed by AIRS. It was found that the OLR data had seasonal variation, and the OLR variation increased with decreasing latitude.

In this paper, through EOF decomposition, the total variance of the first four modes exceeds 70%, but our first mode variance contribution is less than 50%. However, we can find that in the current research process, when researchers used the EOF method to conduct research, the variance of the EOF1 in the research results is basically larger. Examples include Hu's research on EOF analysis to identify the dominant climate patterns responsible for precipitation and then to control environmental factors that control winter precipitation in California [42]; and Wie's research using EOF analysis to find that ENSO has a certain impact on the study of the inter-annual variability of tropospheric ozone in East Asia [43]; their EOF1 is more than 70%, which shows that the EOF1 of their research results has a high reference value. Our low contribution may be due to the complex changes in OLR, which are the result of a combination of factors. At the same time, in this paper, we conduct a linear regression of the times coefficient of EOF decomposition, which can more easily understand its changing trend and facilitate analysis.

At the same time, some scholars have conducted research on the correlation analysis between OLR and some parameters, which coincides with the idea of this paper. For example, Avinash Kumar et al. found that the correlations between BKS and SST, SAT, and OLR were  $-0.75$ ,  $-0.84$ , and  $-0.76$ , respectively; and all passed the 99% significance level test [44]. Li et al. showed that there is an asymmetric relationship between regional average longwave radiation and the SCSSM onset date index [45]. Chaudhari et al. studied sea surface temperature (SST) and OLR in coupled-climate models. At the same time, it was also found that there was a significant negative correlation relationship between high cloud and OLR in the whole monsoon process [46]. In a progressive study of monthly OLR data over 30 years from 1979 to 2013 by Feng et al., the results showed that there was a correlation between convective activity in the western Pacific and OLR during June-August, while the opposite was true between June-July and July-August [47]. Compared with the research of Ye et al. [48], we directly use the data to study the characteristics and potential impact factors, while Ye et al., use the platform model to estimate the value of OLR and its potential impact. In this paper, the linear and spatial correlations of OLR and some parameters are studied, and the idea of looking at the degree of correlation in the whole of East Asia is relatively new.

Although this article analyzes the variation of OLR in East Asia by analyzing the spatiotemporal distribution of year by year, seasonal, and month by month, and analyzes the inter-annual change and time dimension of OLR value, and uses exponential smoothing to test and predict the time series of OLR value, the prediction results are better. At the same time, the correlation analysis was carried out on whether some parameters could affect the OLR, and certain conclusions were obtained. However, there are still some parts

of this paper that have not been studied in depth. For example, due to the complexity of meteorological parameters in the prediction part, we have not considered the influence of other parameters in the prediction model. Therefore, there may be certain errors between the obtained results and the actual values. In addition, in the process of research on correlation, only the correlation between a single parameter and OLR is considered, and the correlation between two or more parameters and OLR is not considered. At the same time, the estimation trend in Figure 5 is not statistically significant, because the amount of data is relatively small; but, this does not mean that the estimation is wrong. Compared with anti-leakage least-squares spectral analysis (ALLSSA), the results obtained by the method we use will have certain limitations [49]. Later, more in-depth research will be carried out.

## 6. Conclusions

Using the exponential smoothing method, empirical orthogonal function, and correlation analysis methods, the spatiotemporal variation of OLR in East Asia and the correlation analysis of the influence of other parameters on OLR were studied; and the following conclusions were drawn:

(1) The spatial distribution of OLR in the Qinghai-Tibet Plateau shows a low-value area whether year-by-year, season, or month. The reason is that as the third pole in the world is the Qinghai-Tibet Plateau, it has complex topography and climate changes. In the range of 10–30° N, it can be found that it may be affected by the western Pacific subtropical high, and a high-value area appears, which is more obvious in spring and winter.

(2) Through the study of the time series, it is found that the change of the time series gradually increases with the decrease of latitude. Meanwhile, with the large amount of cloud near the equator and the proximity of 0–10° N to the equator, part of the OLR propagation is obscured, resulting in less than 10–30° N. It can be seen from the time-latitude map that 2015 was a year with a high OLR value, which may be because 2015 was the longest El Niño “Bruce Lee” and the warmest year in the observation record. It was found that the time series of OLR passed the confidence test and had two abnormal points through prediction, and the deviation was small.

(3) Through EOF analysis, the total variance of the first four modes exceeds 70%, and the trends of the four times coefficient PC values are all decreasing. From the trend of the first 10 years, it is found that only PC2 is increased, and the other three PC are decreased. In the last 9 years, only PC1 is increased, and the other three PC are decreased. Combined with EOF1 and PC1, it is found that the OLR value shows an increasing trend in the range of 0–25° N and 100–135° E in East Asia; and the OLR value shows a decreasing trend in China’s Sichuan, Chongqing, and some waters of the western Pacific Ocean. According to EOF2 and PC2, OLR decreased in South China, Southwest China, Taiwan, East China Sea, Southeast Asia, the Bay of Bengal, and South India; and increased in Northwest China, the Qinghai-Tibet Plateau, and some waters in the Western Pacific.

(4) The correlation study found that the correlation between OLR and the TCWV, AT, and CTT were all highly positive, while there was a high negative correlation with CTP. At the same time, it is found from the spatial correlation study that OLR has similar spatial characteristics with the TCWV and AT, which is basically negative at 0–25° N and basically positive at 30–60° N. The correlation between OLR and CTP is negative in South Korea, North Korea, Japan, and Northern China; and mostly positive in other regions. In Southeast Asia and southern India, the positive correlation is abnormally high, as high as 0.9 or more. In most parts of East Asia, the correlation between OLR and CTT is greater than 0.8, and only a few regions have a low correlation. It is indicating that the change of OLR in the whole of East Asia is greatly affected by CTT and less affected by the other three factors.

**Author Contributions:** C.T.: software, visualization, and writing—review and editing. D.L.: methodology, writing—original draft. X.T.: investigation and resources. F.Z.: investigation and validation. C.D.: methodology, funding acquisition, and validation. All authors have read and agreed to the published version of the manuscript.

**Funding:** This work is supported by the national key research and development program (No. 2019YFA0706004), the Open Project of Advanced Laser Technology Laboratory of Anhui Province (No. AHL2021KF02), the University Natural Science Research Project of Anhui Province of China (No. KJ2019A0103), Anhui Province Key R&D Program of China under Grant (No. 202004i07020011).

**Institutional Review Board Statement:** Not applicable.

**Informed Consent Statement:** Not applicable.

**Data Availability Statement:** We would like to thank the AQUA–AIRS team for providing the necessary datasets used in this study. The version 6.0 level 3 dataset of AIRS is downloaded from <https://disc.gsfc.nasa.gov/datasets>. (Recently accessed date: 23 January 2023).

**Acknowledgments:** We are grateful to the NASA Goddard Space Center for providing the AIRS of OLR, TCWV, AT, CTP, and CTT datasets for this study. We are grateful for the Project supported by the Specialized Research Fund for State Key Laboratories.

**Conflicts of Interest:** The authors declare no conflict of interest.

## References

1. Jin, Z.; Zhang, Y.; Del Genio, A.; Schmidt, G.; Kelley, M. Cloud scattering impact on thermal radiative transfer and global longwave radiation. *J. Quant. Spectrosc. Radiat. Transf.* **2019**, *239*, 106669. [[CrossRef](#)]
2. Karpowicz, B.M.; Mccarty, W.; Wargan, K. Investigating the Utility of Hyperspectral Sounders in the 9.6  $\mu\text{m}$  Band to Improve Ozone Analyses. In Proceedings of the 17th Joint Center for Satellite Data Assimilation Technical Review Meeting and Science Workshop, Washington, DC, USA, 29–31 May 2019.
3. Jing, F.; Zhang, L.; Singh, R.P. Pronounced Changes in Thermal Signals Associated with the Madoi (China) M 7.3 Earthquake from Passive Microwave and Infrared Satellite Data. *Remote Sens.* **2022**, *14*, 2539. [[CrossRef](#)]
4. Wang, T.; Zhou, L.; Tan, C.; Divakarla, M.; Pryor, K.; Warner, J.; Wei, Z.; Goldberg, M.; Nalli, N.R. Validation of Near-Real-Time NOAA-20 CrIS Outgoing Longwave Radiation with Multi-Satellite Datasets on Broad Timescales. *Remote Sens.* **2021**, *13*, 3912. [[CrossRef](#)]
5. Kim, B.-Y.; Lee, K.-T. Using the Himawari-8 AHI Multi-Channel to Improve the Calculation Accuracy of Outgoing Longwave Radiation at the Top of the Atmosphere. *Remote Sens.* **2019**, *11*, 589. [[CrossRef](#)]
6. Alvarez, M.S.; Vera, C.S.; Kiladis, G.N. MJO Modulating the Activity of the Leading Mode of Intraseasonal Variability in South America. *Atmosphere* **2017**, *8*, 232. [[CrossRef](#)]
7. Viana, L.P.; Manco, J.A.A.; Herdies, D.L. Dynamic Characteristics of the Circulation and Diurnal Spatial Cycle of Outgoing Longwave Radiation in the Different Phases of the Madden–Julian Oscillation during the Formation of the South Atlantic Convergence Zone. *Atmosphere* **2021**, *12*, 1399. [[CrossRef](#)]
8. Dewitte, S.; Clerbaux, N. Decadal Changes of Earth’s Outgoing Longwave Radiation. *Remote Sens.* **2018**, *10*, 1539. [[CrossRef](#)]
9. Fajary, F.R.; Hadi, T.W.; Yoden, S. Contributing Factors to Spatio-Temporal Variations of Outgoing Longwave Radiation (OLR) in the Tropics. *J. Clim.* **2019**, *32*, 4621–4640. [[CrossRef](#)]
10. You, J.K.; Dong, K.L. Thermal Comfort and Longwave Radiation over Time in Urban Residential Complexes. *Sustainability* **2019**, *11*, 2251. [[CrossRef](#)]
11. Liu, L.; Zhang, W.; Chen, W.; Wu, R.; Wang, L. Evaluation of FY-3B Reprocessed OLR Data in the Asian—Australian Monsoon Region during 2011–2019: Comparison with NOAA OLR. *J. Meteorol. Res.* **2021**, *35*, 964–974. [[CrossRef](#)]
12. Preusker, R.; Carbajal Henken, C.; Fischer, J. Retrieval of Daytime Total Column Water Vapour from OLCI Measurements over Land Surfaces. *Remote Sens.* **2021**, *13*, 932. [[CrossRef](#)]
13. Chedzey, H.; Menzel, W.P.; Lynch, M. Changes in HIRS Detection of Cloud over Australia from 1985 to 2001. *Remote Sens.* **2021**, *13*, 917. [[CrossRef](#)]
14. Lao, P.; Liu, Q.; Ding, Y.; Wang, Y.; Li, Y.; Li, M. Rainrate Estimation from FY-4A Cloud Top Temperature for Mesoscale Convective Systems by Using Machine Learning Algorithm. *Remote Sens.* **2021**, *13*, 3273. [[CrossRef](#)]
15. Koji, A.K.; Van Malderen, R.; Pottiaux, E.; Van Schaeybroeck, B. Understanding the Present-Day Spatiotemporal Variability of Precipitable Water Vapor over Ethiopia: A Comparative Study between ERA5 and GPS. *Remote Sens.* **2022**, *14*, 686. [[CrossRef](#)]
16. Amoruso, A.; Crescentini, L. Clues of Ongoing Deep Magma Inflation at Campi Flegrei Caldera (Italy) from Empirical Orthogonal Function Analysis of SAR Data. *Remote Sens.* **2022**, *14*, 5698. [[CrossRef](#)]
17. Zhang, T.; Yu, W.; Lu, Y.; Chen, L. Identification and Correlation Analysis of Engineering Environmental Risk Factors along the Qinghai–Tibet Engineering Corridor. *Remote Sens.* **2022**, *14*, 908. [[CrossRef](#)]
18. Heng, Z.; Jiang, X. An Assessment of the Temperature and Humidity of Atmospheric Infrared Sounder (AIRS) v6 Profiles Using Radiosonde Data in the Lee of the Tibetan Plateau. *Atmosphere* **2019**, *10*, 394. [[CrossRef](#)]
19. Strow, L.L.; Hepplewhite, C.; Motteler, H.; Buczkowski, S.; DeSouza-Machado, S. A Climate Hyperspectral Infrared Radiance Product (CHIRP) Combining the AIRS and CrIS Satellite Sounding Record. *Remote Sens.* **2021**, *13*, 418. [[CrossRef](#)]

20. Qin, H.; Kawamura, H. Atmospheric response to a Hot SST Event in November 2006 as observed by the AIRS instrument. *Adv. Space Res.* **2009**, *3*, 395–400. [[CrossRef](#)]
21. Sun, J.; McColl, K.A.; Wang, Y.; Rigden, A.J.; Lu, H.; Yang, K.; Li, Y.; Santanello, J.A., Jr. Global evaluation of terrestrial near-surface air temperature and specific humidity retrievals from the Atmospheric Infrared Sounder (AIRS). *Remote Sens. Environ.* **2020**, *252*, 112146. [[CrossRef](#)]
22. Hwang, J.; Son, S.W.; Martineau, P.; Barriopedro, D. Impact of winter blocking on surface air temperature in East Asia: Ural versus Okhotsk blocking. *Clim. Dyn.* **2022**, *59*, 2197–2212. [[CrossRef](#)]
23. Kwon, E.H.; Sohn, B.J.; Smith, W.L.; Li, J. Validating IASI Temperature and Moisture Sounding Retrievals over East Asia Using Radiosonde Observations. *J. Atmos. Ocean. Technol.* **2012**, *29*, 1250–1262. [[CrossRef](#)]
24. Zhang, H.; Zhao, M.; Chen, Q.; Wang, Q.; Zhao, S.; Zhou, X.; Peng, J. Water and Ice Cloud Optical Thickness Changes and Radiative Effects in East Asia. *J. Quant. Spectrosc. Radiat. Transf.* **2020**, *254*, 107213. [[CrossRef](#)]
25. Jia, X.; Lv, T.; He, F.; Huang, H. Collaborative Data Downloading by Using Inter-Satellite Links in LEO Satellite Networks. *IEEE Trans. Wirel. Commun.* **2017**, *16*, 1523–1532. [[CrossRef](#)]
26. Tang, C.; Liu, D.; Wei, Y.; Tian, X.; Zhao, F.; Wu, X. Spatial-Temporal Mode Analysis and Prediction of Outgoing Longwave Radiation over China in 2002–2021 Based on Atmospheric Infrared Sounder Data. *Atmosphere* **2022**, *13*, 400. [[CrossRef](#)]
27. Gustriansyah, R.; Alie, J.; Suhandi, N. Modeling the number of unemployed in South Sumatra Province using the exponential smoothing methods. *Qual. Quant.* **2022**, *8*, 1–13. [[CrossRef](#)]
28. Chen, J.; Huang, L.; Liu, L.; Wu, P.; Qin, X. Applicability Analysis of VTEC Derived from the Sophisticated Klobuchar Model in China. *ISPRS Int. J. Geo-Inf.* **2017**, *6*, 75. [[CrossRef](#)]
29. Bie, Y.; Li, Z.; Hu, Z.; Chen, J. Queue Management Algorithm for Satellite Networks Based on Traffic Prediction. *IEEE Access* **2022**, *10*, 54313–54324. [[CrossRef](#)]
30. Rubio, L.; Gutiérrez-Rodríguez, A.J.; Forero, M.G. EBITDA Index Prediction Using Exponential Smoothing and ARIMA Model. *Mathematics* **2021**, *9*, 2538. [[CrossRef](#)]
31. Sun, J.; Ding, K.; Lai, Z.; Huang, H. Global and Regional Variations and Main Drivers of Aerosol Loadings over Land during 1980–2018. *Remote Sens.* **2022**, *14*, 859. [[CrossRef](#)]
32. Chen, J.; Jiang, L.; Luo, J.; Tian, L.; Tian, Y.; Chen, G. Characteristics and Influencing Factors of Spatial Differentiation of Market Service Industries in Rural Areas around Metropolises—A Case Study of Wuhan City’s New Urban Districts. *ISPRS Int. J. Geo-Inf.* **2022**, *11*, 170. [[CrossRef](#)]
33. Zhang, S.; Tao, F.; Wu, Q.; Han, Q.; Wang, Y.; Zhou, T. Structural Differences of PM<sub>2.5</sub> Spatial Correlation Networks in Ten Metropolitan Areas of China. *ISPRS Int. J. Geo-Inf.* **2022**, *11*, 267. [[CrossRef](#)]
34. Munagapati, H.; Tiwari, V.M. Spatio-Temporal Patterns of Mass Changes in Himalayan Glaciated Region from EOF Analyses of GRACE Data. *Remote Sens.* **2021**, *13*, 265. [[CrossRef](#)]
35. Bril, A.; Maksyutov, S.; Belikov, D.; Oshchepkov, S.; Yoshida, Y.; Deutscher, N.M.; Griffith, D.; Hase, F.; Kivi, R.; Morino, I.; et al. EOF-based regression algorithm for the fast retrieval of atmospheric CO<sub>2</sub> total column amount from the GOSAT observations. *J. Quant. Spectrosc. Radiat. Transf.* **2017**, *189*, 258–266. [[CrossRef](#)]
36. Peng, Z.; Letu, H.; Wang, T.; Shi, C.; Zhao, C.; Tana, G.; Naizhuo, Z.; Tie, D.; Ronglin, T.; Huazhe, S.; et al. Estimation of shortwave solar radiation using the artificial neural network from Himawari-8 satellite imagery over China. *J. Quant. Spectrosc. Radiat. Transf.* **2019**, *240*, 106672. [[CrossRef](#)]
37. Chae, J.H.; Sherwood, S.C. Insights into Cloud-Top Height and Dynamics from the Seasonal Cycle of Cloud-Top Heights Observed by MISR in the West Pacific Region. *J. Atmos. Sci.* **2010**, *67*, 248–261. [[CrossRef](#)]
38. Shawky, M.; Ahmed, M.R.; Ghaderpour, E.; Gupta, A.; Achari, G.; Dewan, A.; Hassan, Q.K. Remote sensing-derived land surface temperature trends over South Asia. *Ecol. Inform.* **2023**, *74*, 101969. [[CrossRef](#)]
39. Zhai, D.; Zhang, X.; Xiong, P. Detecting Thermal Anomalies of Earthquake Process Within Outgoing Longwave Radiation Using Time Series Forecasting Models. *Ann. Geophys.* **2020**, *63*, PA548. [[CrossRef](#)]
40. Fu, C.C.; Lee, L.C.; Ouzounov, D.; Jan, J.C. Earth’s Outgoing Longwave Radiation Variability Prior to M ≥ 6.0 Earthquakes in the Taiwan Area During 2009–2019. *Front. Earth Sci.* **2020**, *8*, 15. [[CrossRef](#)]
41. Su, B.; Li, H.; Ma, W.; Jing, Z.; Qi, Y.; Jing, C.; Yue, C.; Kang, C. The Outgoing Longwave Radiation Analysis of Medium and Strong Earthquakes. *IEEE J. Sel. Top. Appl. Earth Obs. Remote Sens.* **2021**, *14*, 6962–6973. [[CrossRef](#)]
42. Hu, F.; Zhang, L.; Liu, Q.; Chyi, D. Environmental Factors Controlling the Precipitation in California. *Atmosphere* **2021**, *12*, 997. [[CrossRef](#)]
43. Wie, J.; Park, H.-J.; Lee, H.; Moon, B.-K. Near-Surface Ozone Variations in East Asia during Boreal Summer. *Atmosphere* **2020**, *11*, 206. [[CrossRef](#)]
44. Kumar, A.; Yadav, J.; Mohan, R. Spatio-temporal change and variability of Barents-Kara sea ice, in the Arctic: Ocean and atmospheric implications. *Sci. Total Environ.* **2020**, *753*, 142046. [[CrossRef](#)] [[PubMed](#)]
45. Li, C.; Zheng, Z.; Gu, D.; Lin, A. Asymmetric effects of atmospheric circulation on the South China Sea summer monsoon onset. *Dyn. Atmos. Ocean.* **2019**, *87*, 101099. [[CrossRef](#)]
46. Chaudhari, H.S.; Hazra, A.; Pokhrel, S.; Chakrabarty, C.; Saha, S.K.; Sreenivas, P. SST and OLR relationship during Indian summer monsoon: A coupled climate modelling perspective. *Meteorol. Atmos. Phys.* **2018**, *130*, 211–225. [[CrossRef](#)]

47. Feng, X.; Fan, F. Role of Local Air-Sea Interaction in a Significant Correlation of Convective Activity in the Western Pacific Warm Pool between June and August. *J. Meteorol. Soc. Japan. Ser. II* **2019**, *97*, 955–1008. [[CrossRef](#)]
48. Ye, H.; Guo, H.; Liu, G.; Ping, J.; Zhang, L.; Zhang, Y. Estimating the Earth's Outgoing Longwave Radiation Measured from a Moon-Based Platform. *Remote Sens.* **2021**, *13*, 2201. [[CrossRef](#)]
49. Dastour, H.; Ghaderpour, E.; Zaghoul, M.S.; Farjad, B.; Gupta, A.; Eum, H.; Achari, G.; Hassan, Q.K. Wavelet-based spatiotemporal analyses of climate and vegetation for the Athabasca river basin in Canada. *Int. J. Appl. Earth Obs. Geoinf.* **2022**, *114*, 103044. [[CrossRef](#)]

**Disclaimer/Publisher's Note:** The statements, opinions and data contained in all publications are solely those of the individual author(s) and contributor(s) and not of MDPI and/or the editor(s). MDPI and/or the editor(s) disclaim responsibility for any injury to people or property resulting from any ideas, methods, instructions or products referred to in the content.